Spin-structured multilayer THz emitters by oblique incidence deposition

Cite as: J. Appl. Phys. **133**, 033903 (2023); https://doi.org/10.1063/5.0128437
Submitted: 28 September 2022 • Accepted: 25 December 2022 • Published Online: 17 January 2023

Elias Kueny, Anne-Laure Calendron, Sven Velten, et al.

Journal of Applied Physics ARTICLE scitation.org/journal/jap

Spin-structured multilayer THz emitters by oblique incidence deposition

Cite as: J. Appl. Phys. **133**, 033903 (2023); doi: 10.1063/5.0128437
Submitted: 28 September 2022 · Accepted: 25 December 2022 ·
Published Online: 17 January 2023

Elias Kueny,[1] Anne-Laure Calendron,[2,a)] Sven Velten,[2] Lars Bocklage,[2,3] Franz X. Kärtner,[1,3,4] and Ralf Röhlsberger[2,3,5,6,7]

AFFILIATIONS

[1]Center for Free-Electron Laser Science CFEL, Deutsches Elektronen-Synchrotron DESY, Notkestr. 85, 22607 Hamburg, Germany
[2]Deutsches Elektronen-Synchrotron DESY, Notkestr. 85, 22607 Hamburg, Germany
[3]The Hamburg Centre for Ultrafast Imaging, Luruper Chaussee 149, 22761 Hamburg, Germany
[4]Department of Physics, University of Hamburg, Luruper Chaussee 149, 22761 Hamburg, Germany
[5]Friedrich-Schiller-Universität Jena, Max-Wien-Platz 1, 07743 Jena, Germany
[6]Helmholtz-Institut Jena, Fröbelstieg 3, 07743 Jena, Germany
[7]Helmholtz Centre for Heavy Ion Research (GSI), Planckstr. 1, 64291 Darmstadt, Germany

[a)]**Author to whom correspondence should be addressed:** anne-laure.calendron@desy.de

ABSTRACT

State-of-the-art THz spintronic emitters require a constant magnetic field to saturate their magnetization. We demonstrate that depositing the ferromagnetic layers at oblique incidence confines the magnetization to a chosen in-plane easy axis and maintains the saturation in the absence of an external magnetic field. We use this method to build THz emitters structured as spin valves, for which we use an external magnetic field to turn on and off the emission of THz radiation as well as to change its polarization. We are able to reproduce the THz waveforms by modeling the spin current and the THz propagation through the multilayer system.

I. INTRODUCTION

Spintronic THz emitters sparked interest in the last decade as compact and competitive THz sources.[1] Their simplest form consists of a pair of ferromagnetic|non-magnetic (NM) nanometer-thin layers. When an ultrafast optical pulse is applied on the ferromagnetic (FM) layer, a transient spin current is launched across the interface into the NM layer. The exact mechanism governing the spin transport is still debated.[2–5] In the NM layer, the spin current is converted by the inverse spin-Hall effect[6] (ISHE) into a transverse charge current, which produces a detectable THz pulse.

As the polarization of the THz field depends on the orientation of the magnetization of the FM layer, the efficiency optimization of the emitters requires that the magnetization is saturated. For soft ferromagnets, this demands the presence of a constant external magnetic field, which hinders the miniaturization of the emitters for applications in spin-based electronics. We aim to develop an alternative method to control the magnetization and consequently manipulate the THz emission, for which a constant external field is not necessary to maintain the saturation. To that end, we use oblique incidence deposition (OID) to prepare the FM layers. The same principle has been recently explored by Hewett *et al.*[7] for CoFeB-based bilayer emitters. This deposition technique results in an adjustable magnetic anisotropy, which confines the magnetization to a chosen in-plane easy axis. An external magnetic field is consequently not required to maintain the saturation but is used to switch the magnetization along its easy axis.

More elaborate structures than the bilayer sample have been used to optimize the THz output, pioneered by Seifert *et al.*[8] using trilayer samples in which the FM layer is inserted between two NM layers with opposite ISHE coefficients.[9] Five-layer configurations with two FM layers, which are aligned antiparallel to each other

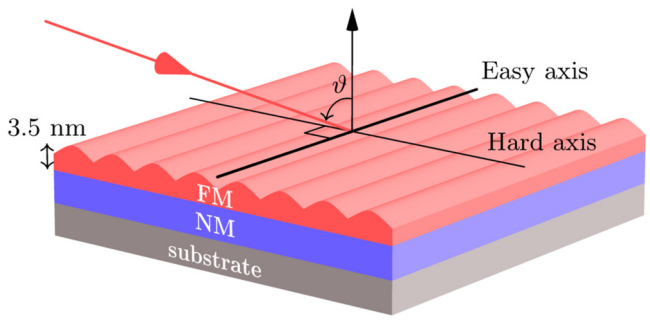

FIG. 1. Schematic of the oblique incidence deposition (OID) process producing a uniaxial magnetic anisotropy in the ferromagnetic (FM) layer via self-shadowing. The angle ϑ is the azimuthal deposition angle. The easy axis of the magnetization is perpendicular to the plane of incidence.

due to an antiferromagnetic interlayer coupling, were shown to double the emitted peak field.[10] Other approaches to control the polarization of the THz include rotating the magnetization of the FM layers with an external magnetic field[11–13] and rotating an AFM|FM sample where exchange bias creates a field-free remanence.[14] Other techniques to modulate the THz radiation include integrating the spintronic emitters on chips,[15] using metamaterials,[16] or using the antiferromagnetic interlayer coupling to form a spin-valve structure that allows to turn on and off the THz output.[17]

Using OID, we developed multilayer spintronic THz emitters containing two uncoupled FM layers, thus removing the need for additional layers to fix the iron's magnetization. The strength and direction of the anisotropy of each layer can be independently chosen at the time of the layer production via the deposition conditions. Hence, the magnetization of each FM layer can be independently switched by a transient external magnetic field of appropriate strength, which is reflected in the properties of the THz emission. With this method, we demonstrate samples with distinct states: the THz emission can be switched on and off or its polarization can be rotated by 90° by changing the strength of the magnetic field. The OID is ensuring a sharp transition between those states and a symmetrical behavior when the magnetic field is swept in both directions. To distinguish the magnetic and optical effects, we simulated the spin current using the model of Rouzegar *et al.*[18] based on the spin accumulation in Fe and calculated the propagation of the emitted THz field.

II. DEPOSITION TECHNIQUE

The samples were prepared by magnetron sputter deposition (see details in Appendix A). In the deposition chamber, the azimuthal and polar angles of deposition can be freely chosen. All samples use iron as the FM layer. The NM materials are sputtered at normal incidence (NID) while oblique incidence deposition (OID) is used for the Fe layers. Below 20 nm, OID creates a wavy modulation of the Fe surface, which induces a uniaxial magnetic anisotropy,[19,20] as illustrated in Fig. 1. In the absence of an external field applied along the hard axis, the magnetization is confined to the easy axis of the layer and a sharp 180° switching behavior is obtained when the external field is reversed. The strength of the magnetic anisotropy is determined by the layer thickness and the azimuthal deposition angle ϑ: previous experiments determined that the anisotropy continuously increases up to 85° of incidence.[21,22] This allows us to tune the coercive field necessary for switching the magnetization of each layer. Additionally, the in-plane orientation of the easy axis is set by the polar deposition angle φ and can be different for each Fe layer. Table I presents the structure of the spintronic emitters analyzed in this manuscript.

TABLE I. Layer composition of the emitters mentioned in the manuscript. The brackets and subscripts in the names of the samples indicate the repetition of layers contributing to the THz emission. The indications in parenthesis serve to disambiguate between samples of identical composition but of different deposition procedure. The arrows indicate the polar direction φ of the Fe deposition and, thus, the axis of the magnetizations, when they are not parallel. Each Fe layer is indicated with the azimuthal angle ϑ of its deposition. The layers in the first column are deposited on a 635 μm Al_2O_3 substrate.

Sample name	Material [ϑ(°)], thickness (nm)						
Fe|W(OID)	MgO	Fe[60]	W				
	2	3.5	2				
Fe|W(NID)	MgO	Fe[0]	W				
	2	3.5	2				
$[Pt\|Fe]_2$	Pt	Fe[60]	MgO	Fe[80]	Pt		
	2	3.5	4	3.5	2		
$[Pt\|Fe\|W]_2$	Pt	Fe[60]	W	Fe[80]	Pt		
	2	3.5	4	3.5	2		
$[Fe\|W]_2$ ⤫	MgO	Fe[60]	W	Fe[80]	MgO		
	2	3.5	4	3.5	2		
$[Fe\|W]_2$	MgO	Fe[60]	W	Fe[80]	MgO		
	2	3.5	2	3.5	2		
$[Fe\|W_{int}]_2$	MgO	Fe[60]	W	MgO	W	Fe[80]	MgO
	2	3.5	2	2	2	3.5	2

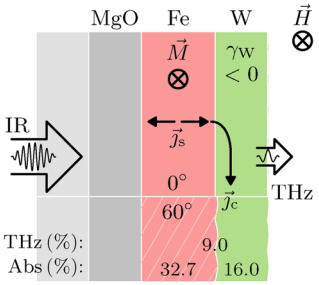

FIG. 2. Schematic of Fe|W(NID) (top part) and Fe|W(OID) (bottom part). The samples are identical except for the fact that the Fe layer of the latter is deposited at 60° oblique incidence. For both samples, the magnetization $\vec{M}$ of the Fe layer aligns on the external magnetic field $\vec{H}$. The absorption of a near-infrared pulse (IR) launches a spin-polarized current $\vec{j}_s$ in the Fe layer, which is converted to a charge current $\vec{j}_c$ by the inverse spin-Hall effect. This transient charge current emits a detectable THz pulse with a linear polarization parallel to $\vec{j}_c$. On the bottom, the proportion of IR energy absorbed in each metallic layer is indicated with respect to the incoming energy (Abs) as well as the proportion of THz energy propagating out of the output (right) interface with respect to the energy emitted by each charge current (THz).

III. DEMONSTRATION OF THE MAGNETIZATION PINNING

To demonstrate the influence of the deposition angle, we manufactured two samples with an identical Al_2O_3|MgO|Fe|W structure (see Fig. 2), named Fe|W(OID) and Fe|W(NID). The Fe layer of the Fe|W(OID) sample is deposited at 60° of incidence, while the Fe layer of the Fe|W(NID) sample is deposited at normal (0°) incidence. In the case of Fe|W(OID), the correlated surface roughness induced by the deposition is transmitted to the above W layer.

Figure 2 illustrates schematically the process of THz emission in both samples. The spin polarization $\vec{\sigma}$ carried by the spin current $\vec{j}_s$ has the same orientation as the magnetization of the layer. The orientation of the charge current $\vec{j}_c$ emitted by the ISHE is defined by the cross product of the latter quantities as well as the sign of the Hall angle γ of the NM layer,[6]

$$\vec{j}_c \propto \gamma \vec{j}_s \times \hat{M}. \tag{1}$$

Due to the small spin-Hall angle of Fe,[1] we assume that only the NM layers contribute to the THz emission.

The behavior of the magnetization when applying an external magnetic field was measured by two methods: using the magneto-optical Kerr effect (MOKE) and via the detection of the emitted THz pulse (see details about the setup in Appendix B). In the case of the THz emission, the inhomogeneous wave equation[23]

$$\vec{\nabla} \times (\vec{\nabla} \times \vec{E}(\omega)) + k^2(\omega)\vec{E}(\omega) = -\frac{iZ_0\omega}{c} j_c(z, \omega) \tag{2}$$

results in a 1D system and, assuming a point source at $z = 0$, in the emitted electric field being proportional to the local current,

$$E_0(z = 0, \omega) = j_c(\omega)Z_0/(2n_{NM}(\omega)). \tag{3}$$

After integration of the charge current in the NM layer and propagation of the field outside of the sample, we expect according to Eqs. (1) and (3) that the amplitude of the measured electric field scales with the spin current and, thus, with the overall magnetization state of the FM layer.

Figure 3(a) shows a MOKE measurement of the hysteresis loop of both samples. Fe|W(NID) has a small coercivity and

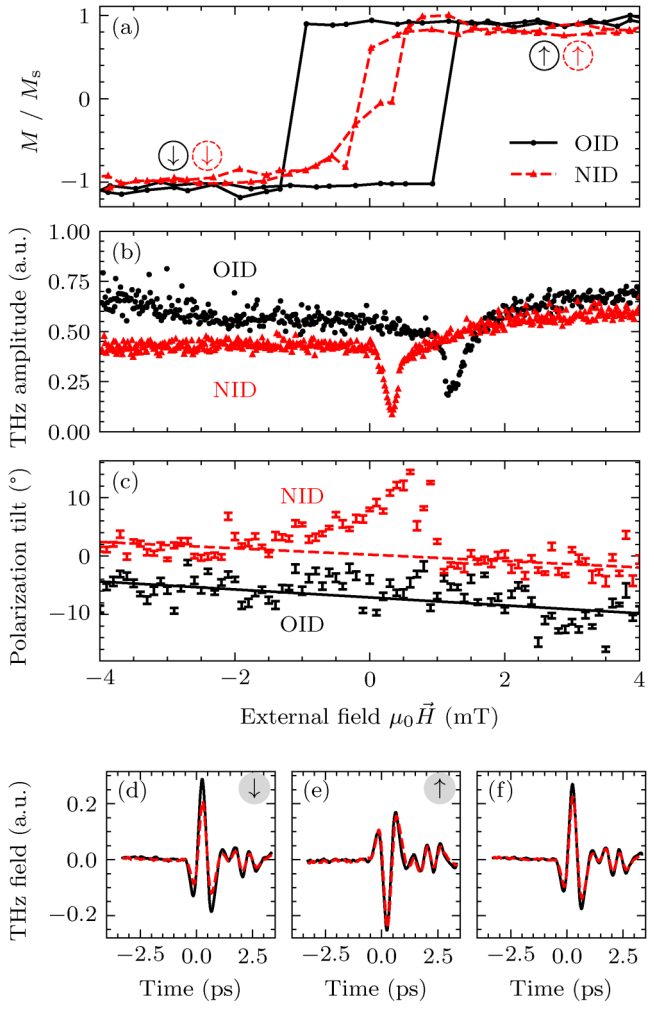

FIG. 3. Comparison of the samples Fe|W(OID) (solid black line) and Fe|W(NID) (dashed red line). (a) Hysteresis curves measured along the easy axis of Fe|W (OID). The circled arrows illustrate the magnetization state of each sample at the indicated field. (b) Peak-to-peak amplitude of the THz waveforms generated by each sample. Only the component normal to the external field $\vec{H}$ was measured. (c) Angle of the linear fit of the polarization ellipse of the THz waveforms. The length of the error bars denotes the standard deviation of the fit residuals. The lines are a guide to the eye. (d) and (e) Averaged electro-optic sampling traces of the THz waveform taken under 0 mT (↓) and above 3 mT (↑). (f) Difference of the waveforms of both magnetization directions showing the pure magnetic contribution (rescaled by a factor 1/2).

switches progressively following the magnetic field. Fe|W(OID) shows on the contrary a behavior close to an ideal hard magnet when the field is applied along its easy axis: it has a coercivity of 1 mT and retains its saturation magnetization until the external field exceeds the OID-induced anisotropy, at which point it switches abruptly. Both behaviors are reflected in the THz emission. The THz waveforms were measured by electro-optical sampling (EOS) while incrementing the strength of the external magnetic field along the lower branch of the hysteresis curve. In Fig. 3(b), the amplitude of the emitted THz follows the absolute magnetization shown in the MOKE curve: the amplitude is overall constant while the magnetization is saturated and decreases for both samples as the magnetization switches. However, the switching process happens differently for both samples. Figures 3(d) and 3(e) show the average waveforms in both magnetization directions. The pure magnetic contribution to the THz signal is obtained from their difference in Fig. 3(f). Both samples emit similar single-cycle THz pulses with a spectrum extending up to 2 THz. The carrier envelope phase (CEP) of the pulses reverse following the magnetization as expected from Eq. (1). The THz radiation emitted via the ISHE is expected to be linearly polarized, perpendicularly to the sample magnetization. The polarization of the THz radiation was found linear and Fig. 3(c) shows its angle. The THz radiation emitted by Fe|W(OID) has a constant polarization, which indicates that the axis of the magnetization is stable. We attribute the overall downward trend to a slight change in the alignment of the collecting optics in the THz detection setup when the external field is swept. By contrast, the polarization of the THz emitted by Fe|W(NID) rotates when the field strength is reduced and reaches a maximum of 15° at 0.6 mT, before coming back to its original angle when the magnetization is again saturated. This shows that while the decrease in THz amplitude of both samples suggests that the magnetization of the Fe layer breaks into domains in both cases during its switching, the unconfined magnetization of Fe|W(NID) is free to rotate to satisfy small local anisotropies. Conversely, the preservation of the THz polarization in Fe|W(OID) in the absence of magnetic field is coherent with our expectation that the domains stay magnetized along the OID-induced easy axis.

Taken together, the measurements in Fig. 3 show that due to the anisotropy of the OID layer, the magnetization is effectively confined along the easy axis. The resulting remanent magnetization renders an external magnetic field unnecessary for the generation of THz pulses or to maintain a well-defined polarization once the sample has been saturated. In addition, while the transmission of the spin current through the FM|NM interface has been shown to heavily depend on the surface quality,[24] the additional roughness created by the OID process did not diminish the amplitude of the emitted THz.

IV. SIMULTANEOUS CONTROL OF TWO FM LAYERS

As the coercivity of an OID layer depends on the azimuthal deposition angle ϑ, it is possible to design samples with two uncoupled FM layers deposited at different angles and, thus, switching at different fields.[21,22] This way, any combination of their magnetizations is accessible at a certain magnetic field. The remanence provided by the OID process ensures that the sample stays in this magnetization state if the external field is removed. Similarly to the structure of spin valves, these samples have two distinct total magnetization states: parallel (↑↑ or ↓↓) and antiparallel (↑↓ or ↓↑).

We manufactured two samples with a symmetrical Al_2O_3|Pt|Fe|NM|Fe|Pt structure, where the central NM layer is W for the $[Pt|Fe|W]_2$ sample and MgO for the $[Pt|Fe]_2$ sample, shown in Figs. 4(a) and 4(b), respectively. Each half of $[Pt|Fe|W]_2$ takes advantage of a NM|FM|NM structure where both NM layers have an opposite spin-Hall angle, allowing for the constructive superposition of the emitted THz radiation.[8,25] For both samples, the polar deposition angle was kept constant so the easy axes of the Fe layers are parallel, while the first Fe layer was deposited at a lower azimuthal angle than the second, giving it a lower coercivity. To minimize the interlayer coupling, we found using a central 2 nm-thick W layer more successful than a Pt layer, as also reported by Schneider *et al.*[26] Because of the mirror symmetry of the sample structure, the charge currents from each half are parallel when the magnetizations are antiparallel, as both $\vec{j}_s$ and $\hat{M}$ in Eq. (1) have opposite signs. In this configuration, the THz emission is maximized. On the contrary, when the magnetizations are parallel, the

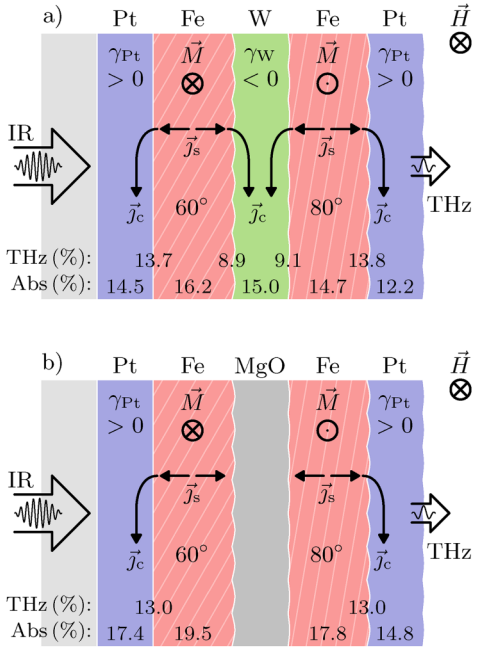

FIG. 4. Schematic of (a) $[Pt|Fe|W]_2$ and (b) $[Pt|Fe]_2$. The Fe layers are deposited at different angles so that the magnetization $\vec{M}$ of the leftmost ones switches first when the external magnetic field $\vec{H}$ is reversed. The absorption of a near-infrared pulse (IR) launches spin-polarized currents $\vec{j}_s$ in the Fe layers, which are converted to charge currents $\vec{j}_c$ by the inverse spin-Hall effect. In the represented state, the antiparallel magnetizations translate in the constructive addition of all THz radiation. On the bottom, the proportion of IR energy absorbed in each metallic layer is indicated with respect to the incoming energy (Abs) as well as the proportion of THz energy propagating out of the output (right) interface with respect to the energy emitted by each charge current (THz).

emitted field adds up destructively and we anticipate a strong attenuation of the measured THz signal.

Figure 5(a) shows the hysteresis curves measured by MOKE of $[Pt|Fe|W]_2$, $[Pt|Fe]_2$, as well as Fe|W(OID) for comparison. Due to changes in the setup, the EOS amplitudes are not directly comparable between sections of this article. Samples with two FM layers are characterized by a switching in two steps. $[Pt|Fe|W]_2$ (solid black lines) shows two parallel magnetization states (labeled ⇓⇓ and ⇑⇑) when the external field exceeds ±6 mT. The opposite charge currents in each half of the sample generate THz emissions that almost completely cancel each other, as shown in Fig. 5(b). When following the lower branch of the hysteresis curve, the first Fe layer switches at 2 mT and the second at 6 mT. In between, the total magnetization of the sample is suppressed, but the four Fe|NM interfaces generate THz radiation constructively. $[Pt|Fe]_2$ behaves in a similar way, with the difference that only the two Fe|Pt

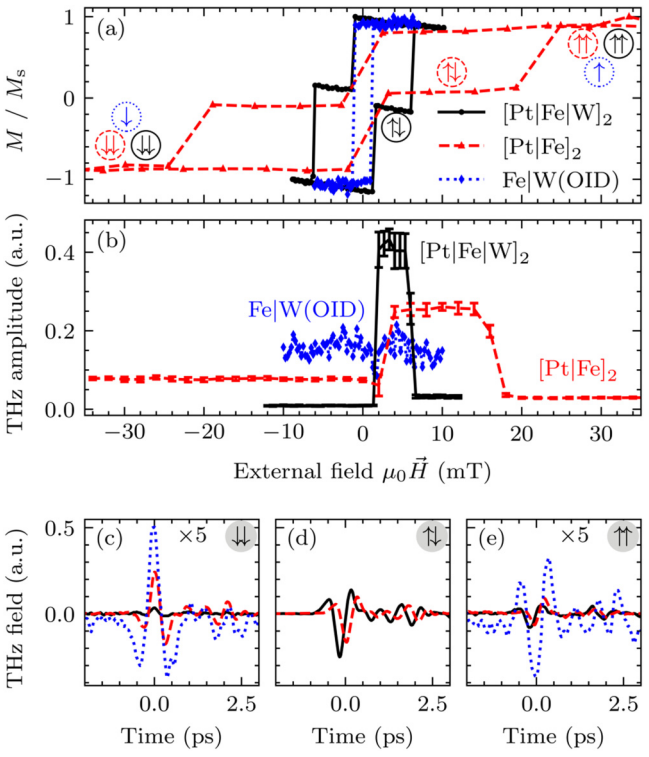

FIG. 5. Comparison of the samples $[Pt|Fe|W]_2$ (solid black line), $[Pt|Fe]_2$ (dashed red line), and Fe|W(OID) (dotted blue line). (a) Hysteresis curves measured by MOKE along the easy axis of the samples. The circled arrows illustrate the magnetization state of each sample at the indicated field. (b) Peak-to-peak amplitude of the THz waveforms generated by each sample. Only the component normal to the external field $\vec{H}$ was measured. The sample magnetization was saturated at $\vec{H} = -40$ mT before progressively increasing the external field. (c)–(e) Electro-optic sampling traces of the THz waveform taken at the external field values indicated by the arrows in (a). Waveforms in parallel states [⇓⇓ in (c) and ⇑⇑ in (e)] are upscaled by a factor 5. Only the five-layer samples have an antiparallel state in (d).

interfaces contribute to THz generation. As MgO is an insulator, there is no direct coupling between the two FM layers, which increases the range over which the sample can be in the antiparallel configuration to 16 mT. However, the THz suppression in the parallel magnetization state in Figs. 5(c) and 5(e) is less complete than for $[Pt|Fe|W]_2$. The same principle was used by Fix *et al.*[17] in samples where one Fe layer has a pinned magnetization while the second is free, creating a smooth transition between the two states.

In the antiparallel configuration, $[Pt|Fe]_2$ and $[Pt|Fe|W]_2$ emit more THz radiation than Fe|W(OID), but only by a factor of 1.6 and 2.7, respectively, showing that increasing the number of ferromagnetic layers comes with a diminishing THz emission efficiency. We performed simulations of those samples to understand the behavior of the THz output and verify whether this loss of efficiency is fully explained by the absorption of the THz as well as the reduced IR power reaching the second Fe layer. On one hand, we used the recent theory of Rouzegar *et al.*[18] to calculate the spin current, based on the principle that $\vec{j}_s$ is produced by a transient spin voltage in the FM layer. On the other hand, we used a transfer-matrix approach to reproduce the optical propagation of the IR pump and the generated THz field out of each sample. The core equation providing the normalized spin current is[18]

$$j_s(t) \propto \Phi(t)[A_{es}\exp(-\Gamma_{es}t) - A_{el}\exp(-\Gamma_{el}t)] \otimes P(t), \qquad (4)$$

where $A_{es} = (\Gamma_{es} - R\Gamma_{el})/(\Gamma_{es} - \Gamma_{el})$ and $A_{el} = (\Gamma_{el} - R\Gamma_{es})/(\Gamma_{es} - \Gamma_{el})$. At $t = 0$, the Heaviside step function $\Phi(t)$ causes the instantaneous generation of the spin current. Its decay is controlled by the electron-spin and electron-lattice relaxation times Γ_{es}^{-1} and Γ_{el}^{-1}, respectively. The bandwidth is then reduced by the convolution with the pump resolution $P(t)$. Finally, $R = (C_e^F + C_e^N)/(C_e^F + C_e^N + C_l^F + C_l^N)$ is the ratio of the electronic and total heat capacities of the combined pair of FM and NM layers. For each interface, we normalized j_s given by Eq. (4) by the fraction of IR power absorbed in the relevant Fe layer and then used Eqs. (1) and (3) to obtain the THz field at the interface. We then calculated the frequency-dependent transfer functions of the THz propagation out of the sample and of the EOS process to estimate the measured signal. The only free parameter was Γ_{es}, which was fitted to match the peak frequency of the measured spectrum and a global amplitude. The details of our implementations can be found in Appendix C.

We calculated that 32.7 % of the IR power is absorbed in the Fe layer of Fe|W(OID), 30.9 % in the two Fe layers of $[Pt|Fe|W]_2$ combined, and 37.3 % in those of $[Pt|Fe]_2$ combined, as indicated on Figs. 2 and 4. While in the five-layer samples more layers generate a spin current, the pump power is diluted and individual Fe layers generate a weaker spin current, reducing the benefit of stacking layers. By contrast, the THz propagation is positively affected by the increase in layers as the sample acts like a resonant cavity:[8] while 9.0 % of the emitted THz energy escapes the Fe|W(OID) sample though the interface opposed to the substrate, this number rises to up to 13.8 % in $[Pt|Fe|W]_2$.

As the THz amplitude is affected by the transparency of the FM|NM interfaces,[27] we used Fe|W(OID) and a similar sample, where W is replaced by Pt to calibrate the emission ratio of a Fe|W interface compared to a Fe|Pt interface. This effective emission

ratio takes into account the spin-Hall angle of the NM layer as well as the transmission of the spin current through the Fe|NM interface,

$$[\gamma_{\mathrm{Pt}} t_{j_s}(\mathrm{Pt})]/[\gamma_{\mathrm{W}} t_{j_s}(\mathrm{W})] = -2.60. \quad (5)$$

Figures 6(a) and 6(b) show the waveform and spectrum of Fe|W(OID), respectively. We use the amplitude of its waveform as a reference to scale the simulations, and the transfer function of the detector is calculated from its spectrum. Our pump pulse duration of 40 fs limits the $1/e^2$ bandwidth of the emitted THz radiation to 9 THz (see Fig. 9). The bandwidth of the measured signal is then further reduced during EOS to 2.2 THz.

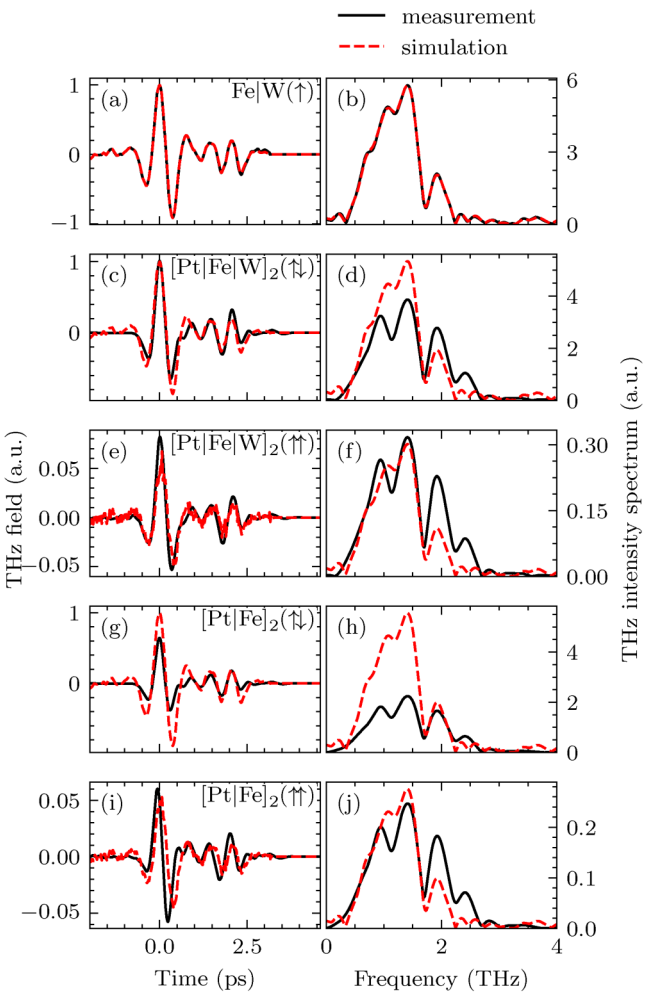

FIG. 6. Comparison of the measured (solid black line) and calculated (dashed red line) THz output of Fe|W(OID) [(a) and (b)], $[Pt|Fe|W]_2$ [(c)–(f)], and $[Pt|Fe]_2$ [(g)–(j)]. The (c) and (g) rows correspond to the antiparallel magnetization state of their respective samples, while the (d) and (i) rows correspond to their parallel state. The simulations were scaled so that the peak-to-peak amplitude of Fe|W(OID) matches the measurement.

We used the result from Eq. (5) to simulate the next samples. Figures 6(d)–6(f) show $[Pt|Fe|W]_2$, whereas Figs. 6(g) to 6(i) show $[Pt|Fe]_2$. Those samples have higher-frequency components, which are not reproduced by the simulation and are coming from the ringing after the main pulse. The CEP of the simulated waveforms is fairly well matching the measurements. In the antiparallel magnetization configuration, the simulated amplitude is too high for both samples, particularly $[Pt|Fe]_2$. This could point to Eq. (5) being too high, which means that the conversion from $\vec{j}_s$ into $\vec{j}_c$ for Fe|Pt interfaces is lower than expected in five-layer samples.

The amplitudes of the simulated waveforms in the parallel configuration, however, match those of the measurements. As the waveform of both configurations is calculated from the same emitted THz fields only with different polarities, this means that the simulation overestimates in both cases the reduction in amplitude in the parallel configuration compared to the antiparallel one. In the parallel configuration, the relative amplitudes of each THz emission are crucial. One potential cause of imbalance between the two halves of a sample is the impedance of the FM layer. As the pump beam is polarized so that its magnetic field is along the OID axis, we assume that the magnetization of the Fe layer is always fully saturated and it has a relative permeability $\mu_r = 1$. If this assumption is inexact, it can cause an increased THz emission in the parallel configuration. Another potential cause of imbalance is the difference in the surface quality of the Fe|NM interfaces: the first NM layer is deposited on the polished substrate, while the others are deposited above one or two OID layers, which have a rougher surface. As the surface quality influences the transmission of the spin current,[24] this would reduce the amount of THz emitted by the second half of the sample. In addition, the fact that the Fe layers are deposited on different materials was reported to influence their saturation magnetization.[17] This can both render the ratio in Eq. (5) inexact and further imbalance the THz emitted in both halves of the sample, impairing the extinction in the parallel state.

V. PERPENDICULAR FM LAYERS

After demonstrating the ability to control two FM layers with a field applied along their common easy axis, we investigate the possibility of manipulating two FM layers with orthogonal easy axes. For this, we manufacture a sample with a symmetrical Al_2O_3|MgO|Fe|W|Fe|MgO structure, where the polar deposition angle was +45° for the first Fe layer and −45° for the second. This $[Fe|W]_2$ ⤫ sample is shown in Fig. 7. The central layer is thickened to 4 nm to avoid spin-transfer torque between the FM layers. The external magnetic field is applied as before along the direction of a polar axis of 0°, now diagonal to both easy axes.

The MOKE curve in Fig. 8(a) shows the same two-step switching as the previous samples, but has an additional slope due to the mixing of the easy-axis and hard-axis magnetizations. It shows that as the field strength increases in the ⤫ and ⤬ configurations, the magnetization tends to rotate away from the easy axes to align with the field. In the first approximation, we can consider that at a low field, there is a constant 90° angle between the

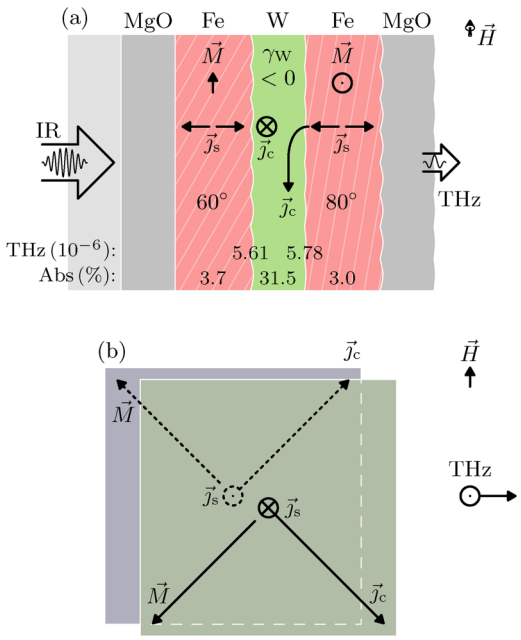

FIG. 7. Schematic of [Fe|W]$_2$ ⤫ seen (a) in plane and (b) from the normal to the plane. The Fe layers were deposited by OID with polar angles of $\pm 45°$ so that their magnetizations $\vec{M}$ are always perpendicular. The absorption of a near-infrared pulse (IR) launches spin-polarized currents $\vec{j}_s$ in the Fe layers, which are converted into two perpendicular charge currents $\vec{j}_c$ by the inverse spin-Hall effect. The total emitted THz is the sum of the two perpendicularly polarized fields generated by the transient charge currents. Its polarization switches from parallel to $\vec{H}$, to perpendicular (as depicted) as the magnetization switches. On the bottom, the proportion of IR energy absorbed in each metallic layer is indicated with respect to the incoming energy (Abs) as well as the proportion of THz energy propagating out of the output (right) interface with respect to the energy emitted by each charge current (THz). In (b), each square represents the vectors associated with one Fe layer.

magnetization of each layer. This translates into two perpendicularly polarized components of the THz: instead of changing the amplitude of the THz pulse, the switching of the magnetization rotates its polarization. As the sample is nanometer-thin, both the delay in IR absorption and the THz propagation lead to a negligible phase difference between both components. The THz is then expected to be linearly polarized. At higher field strengths (⤫ and ⤬ magnetization configurations), the polarization is expected to be parallel to the external field, independently of the side of the sample along which the field is applied.

We measured EOS traces of two orthogonal components of the THz field, allowing us to reconstruct its three-dimensional electric field while scanning the lower branch of the hysteresis curve. The orientation of the THz polarization is shown in Fig. 8(c). We see the same downward trend of the polarization as already observed for Fe|W(OID) in Fig. 3(c), which is not specific to this sample. As expected, the switching of the magnetization between 1.5 and 3.5 mT corresponds to a sharp rotation of the polarization close to 90°. Figure 8(b) shows the peak amplitude of the THz

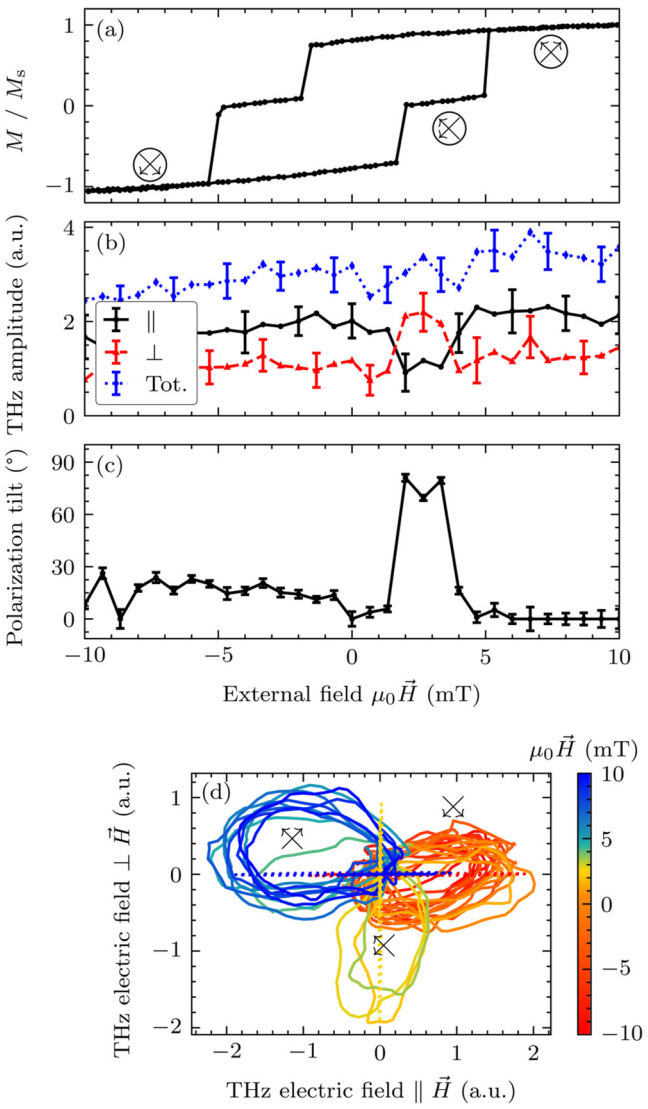

FIG. 8. (a) Hysteresis curve of [Fe|W]$_2$ ⤫ measured at 45° between both easy axes. The circled arrows indicate the magnetization of each Fe layer. (b) Peak-to-peak amplitude of the components of the THz waveforms parallel to $\vec{H}$ (∥, black solid line) and perpendicular to $\vec{H}$ (⊥, dashed red line) as well as their sum (dotted blue line), calculated from the measured diagonal components. The error-bars are spaced every third data point for visibility. The error bars are the pooled standard deviations of the amplitudes, calculated using the standard deviation of the peak diagonal fields when repeating the measurement. (c) Fit of the orientation of the THz polarization extracted from (d). A polarization of 0° means parallel to $\vec{H}$. (d) Projection of the THz electric field in the plane normal to the propagation direction. Each ellipse represents the average experimental waveform at a given magnetic field. The dotted lines represent the simulated polarization ellipses.

waveforms along the parallel and perpendicular directions to the external field as well as the amplitude of the full waveform. The rotation of the polarization is visible as the amplitude of the parallel and perpendicular components changes. The total THz amplitude

is, however, not affected. Outside this range, their amplitudes are stable within the experimental error, indicating that the magnetizations are not significantly rotating out of their easy axes.

We notice that both polarization components are non-zero, indicating that the THz polarization is tilted compared to the field. Figure 8(d) shows the polarization ellipses formed at each magnetic field by the projection of the THz electric field onto the plane normal to the propagation direction. There are three distinct groups of ellipses, corresponding to the three states of the sample. As seen from Fig. 8(b), the THz polarization is always elliptical instead of linear. Since we measured the THz polarization of [Pt|Fe|W]$_2$ and [Pt|Fe]$_2$ to be linear, the cause of the ellipticity for [Fe|W]$_2$ ⤫ is in the orthogonality of the easy axes. We do not expect the mechanism of emission in this sample to be different from the others, in which case only three elements control the polarization: the spin polarization of the spin current, the orientation of the charge currents, and the phase between the two THz emissions. The phase difference between the components due to the propagation of the IR pump as well as the emitted THz is negligible. This includes the birefringence caused by the grating-like interfaces of the OID layers.[28] We estimate that a delay on the order of 100 fs between the components is necessary to optically reproduce the observed ellipticity. We, thus, do not expect it to be caused by an optical phase difference. To also exclude a time-dependence of the charge currents, we calculated the Lorentz force exerted by the THz field emitted at one Fe|W interface on the electrons of the charge current at the other Fe|W interface and found an in-plane deviation of the current direction inferior to 0.1 %. This leaves the possibility of a time variation of the spin polarization, which has been observed in specific conditions,[7] but which we are unable to explain in this case.

VI. CONCLUSION

Using oblique incidence deposition, we tested different geometries of spintronic THz emitters, where the magnetization of each ferromagnetic layer is confined to a chosen in-plane easy axis with a different anisotropy. These samples have the advantage that the magnetization stays saturated when the external magnetic field is removed. We demonstrated the ability of samples with two uncoupled ferromagnetic layers to switch their magnetization independently and, thus, manipulate the way the THz emission from both layers interferes constructively or destructively. When both easy axes are orthogonal, the THz radiation can be switched between p and s polarizations using the external field, although the polarization becomes elliptical. When both easy axes are parallel, the THz emission can be switched on and off on a pulse-to-pulse basis by switching the external field. While other approaches are available,[7,17] OID layers make the emitters less sensitive to the strength and direction of the magnetic field and allow us to choose the direction of the in-plane magnetization of each layer. Due to the distribution of the pump power into more layers, we found that the THz output of five-layer samples with two ferromagnetic layers of antiparallel magnetization was equivalent to that of the corresponding three-layer sample with a single ferromagnetic layer. Such a sample offers a practical way to generate on-demand THz pulses by changing the alignment of the two magnetizations.

ACKNOWLEDGMENTS

This work was supported/funded by the Cluster of Excellence "CUI: Advanced Imaging of Matter" of the Deutsche Forschungsgemeinschaft (DFG) (EXC 2056, Project No. 390715994). Part of this work was made possible by the post-doc grant from the Helmholtz association (P303) of A.-L. Calendron. The authors heartily thank the mechanical engineers T. Tilp and A. Berg for their support as well as G. Meier for proofreading the manuscript.

AUTHOR DECLARATIONS

Conflict of Interest

The authors have no conflicts to disclose.

Author Contributions

Elias Kueny: Formal analysis (lead); Investigation (equal); Methodology (supporting); Software (supporting); Validation (equal); Visualization (lead); Writing – original draft (lead). **Anne-Laure Calendron:** Conceptualization (supporting); Formal analysis (supporting); Funding acquisition (equal); Investigation (equal); Methodology (lead); Project administration (lead); Software (lead); Supervision (lead); Validation (equal); Writing – review & editing (lead). **Sven Velten:** Resources (lead); Writing – review & editing (supporting). **Lars Bocklage:** Conceptualization (lead); Methodology (supporting); Resources (supporting); Writing – review & editing (supporting). **Franz X. Kärtner:** Conceptualization (supporting); Funding acquisition (equal); Writing – review & editing (supporting). **Ralf Röhlsberger:** Conceptualization (supporting); Funding acquisition (supporting); Writing – review & editing (supporting).

DATA AVAILABILITY

The data that support the findings of this study are available from the corresponding author upon reasonable request.

APPENDIX A: SAMPLE FABRICATION

All samples are prepared by magnetron sputter deposition with a base pressure under 7×10^{-7} mbar. The substrate is a double-polished 1×1, 635 µm -thick (0 0 0 1) Al_2O_3 wafer. The FM layers are sputtered with elementary iron into a polycrystalline α-Fe phase, although lattice defects are expected due to the low thickness. The sputtering was done at normal incidence, except for most Fe layers, which were deposited with an azimuthal angle of $\vartheta = 60°$ or 80° and a polar angle of $\varphi = 0°$ or $\pm 45°$ with respect to the substrate edge. When deposited in an oblique incidence angle, the sample was turned by $\varphi = 180°$ halfway through the deposition process to prevent any thickness gradient. The roughness of the layers deposited above the OID iron layers reaches 1.2 nm.[21] For more details on the surface properties of similar samples, we refer the reader to Willing *et al.*[22] and Schlage *et al.*[21] A list of all samples is presented in Table I.

APPENDIX B: EXPERIMENTAL SETUP

The spintronic emitters are illuminated by 800 nm, 35 fs-long pulses at 1.5 kHz , with a typical energy in front of the sample of about 800 μJ with a 8.4 mm-diameter flat-top intensity distribution. The samples are glued on a non-magnetic copper holder with the substrate side facing the IR beam, centered in an electromagnetic yoke producing a magnetic field homogeneous over the illuminated surface. Unless mentioned otherwise, the easy axis of the samples is aligned along the axis of the magnetic field. To ensure the reproducibility of the magnetic states of the yoke and the samples, their magnetization is saturated at the beginning of every measurement by applying the same current in the electromagnet, generating a −80 mT field on the samples. The magnetic field is then progressively scanned in the positive direction while measuring the THz. The whole scan including the saturation of the yoke is repeated typically 15–30 times successively and averaged to reduce the influence of short-term energy fluctuations of the laser. The correspondence between the electric current applied to the electromagnet and the magnetic field at the illuminated spot was measured with a Hall sensor.

The measurement of the THz radiation is done by electro-optical sampling. A 200 μJ part of the IR beam is further compressed down to 20 fs as published in Calendron *et al.*[29] to be used as a probe. A Germanium film filters the IR pump transmitted through the spintronic emitters, absorbing an estimated half of the THz energy. The transmitted THz is collected and refocused by a pair of off-axis parabola with reflected focal lengths of 6 and 4 in., respectively. A 500 μm-thick ⟨1 1 0⟩-cut ZnTe crystal is mounted in the focus. The probe is transmitted through an opening in the second parabola and superposed to the THz focus on the crystal. A constant polarization of the THz is ensured by a grid polarizer. The probe transmitted through the ZnTe crystal is sent onto a balanced detector to measure the rotation of its polarization induced by the THz field. A motorized translation stage is used to scan the delay of the probe and the signal from the difference of the balanced detectors is acquired using a lock-in amplifier. Due to the influence on the EOS amplitude of the pump and probe energy, the THz amplitude is not comparable between different sections of the manuscript.

In the case of the polarization measurements, a first THz polarizer transmitted the $\pm 45^\circ$ components while a second polarizer re-established the vertical polarization on the EOS crystal to ensure a constant efficiency. The horizontal and vertical components of the electric field were reconstructed from both diagonal components. Except in the case of $[Fe|W]_2$ ⤫, the THz polarization was always linear. The tilt of the polarization was obtained as the linear fit of the polarization ellipse, weighted by the standard deviation of the electric field components. The samples were mounted with a maximum tilt of 1°. The uncertainty on the direction of the easy axis during the deposition process is 2°. The downward trend of the measured polarizations in Figs. 3(c) and 8(c) is suspected to come from a misalignment of the THz beam on the off-axis parabolas.

The THz intensity was too low to be measured by our THz detectors. Our estimation places it at the nJ-level, coherent with the conversion efficiency from the IR of 10^{-6} as measured by Seifert *et al.*[25]

APPENDIX C: SIMULATIONS

We based our simulations on the recent work of Rouzegar *et al.*[18] They developed a model based on the idea that ultrafast demagnetization of a FM layer and spin transport though an FM|NM interface both[30] predominantly arise from a spin voltage $\Delta\mu_s$ induced by the ultrafast pump: $j_s(t) \propto \dot{M}(t) \propto \Delta\mu_s(t)$. As the pump is absorbed, the spin voltage is created by the spin-dependent change in chemical potential. Assuming that the temperature is instantly equilibrated within the electrons bath, they model the spin voltage as instantly rising and decaying by equilibration of the electrons with the lattice and the spin degree of freedom with time constants of Γ_{el}^{-1} and Γ_{es}^{-1}, respectively. Equation (4) gives the resulting time evolution of the spin current. The electron-lattice equilibration for the FM|NM system can be calculated as $\Gamma_{el} = (G_{el}^F + G_{el}^N)/(C_e^F + C_e^N)$.

We, thus, need for all NM and FM materials the specific heats of the electrons C_e and lattice C_l as well as their coupling constant G_{el}. They are themselves temperature-dependent.[31] For numerical simplicity, we used constant parameters for input in Eq. (4), corresponding to the peak electronic temperature calculated from the three-temperature model. Those parameters are given in Table II. We calculated the electronic temperature using the three-temperature model, following a system of equations adapted from Chimata *et al.*[32] and Kirilyuk *et al.*,[33]

$$\frac{dT_e}{dt} = \frac{1}{C_e}[-G_{el}(T_e - T_l) - G_{es}(T_e - T_s) + P(t)], \tag{C1a}$$

$$\frac{dT_s}{dt} = \frac{1}{C_s}[-G_{es}(T_s - T_e) - G_{sl}(T_s - T_l)], \tag{C1b}$$

$$\frac{dT_l}{dt} = \frac{1}{C_l}\left[-G_{el}(T_l - T_e) - G_{sl}(T_l - T_s) - h\pi w_0^2(T_l - T_{BG})\right], \tag{C1c}$$

where h represents the losses to the environment, $P(t)$ the instantaneous laser power, w_0 the beam radius size, and T_{BG} the environment temperature, considered equal to the steady-state temperature of the samples.[32,33] The parameters for Eq. (C1) are given in Table III. The laser power $P(t)$ absorbed in a FM layer was calculated from the difference of the Poynting vectors at each interface,[34] using the generalized Fresnel coefficients for magnetic and lossy

TABLE II. Input parameters for Eq. (4). C_e, and G_{el} were taken at $T_e = 5000$ K for Fe, 4000 K for Pt, and 7000 K for W.

	Unit	Fe	Pt	W
C_e	10^6 J m^{-3} K^{-1}	2.25[36]	3[37]	0.7388[38]
C_l	10^6 J m^{-3} K^{-1}	2.2[32]	2.85[37]	2.4554[38]
G_{el}	10^{17} W m^{-3} K−1	38[31]	1.3[31]	1.3[31]
λ	10^{-9}m	…	1.2[39]	1.4[39]
γ		…	0.051[40]	−0.33[41]

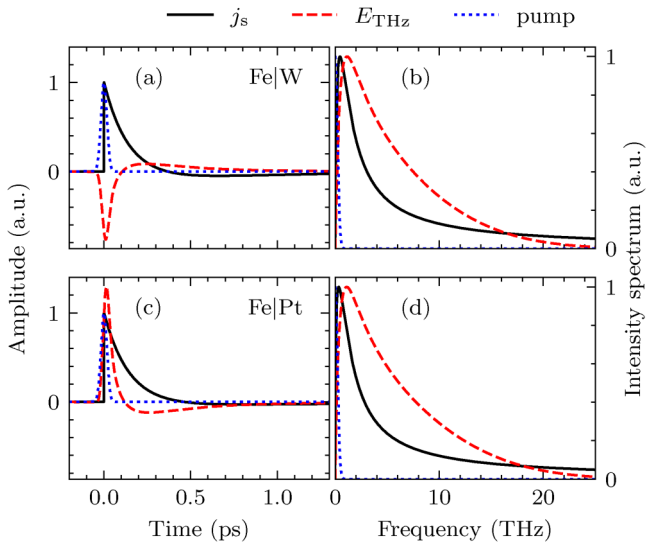

FIG. 9. Simulation of the spin current (black solid curve) and emitted THz (red dashed curve) for both types of interfaces. The relaxation times are $\Gamma_{es}^{-1} = 143$ fs and $\Gamma_{el}^{-1} = 1.3$ ps. Here, j_s is given before convolution with the pump $P(t)$ (blue dotted curve).

media,[35]

$$r_{1\to2} = \frac{\mu_2 n_1 - \mu_1 n_2}{\mu_2 n_1 + \mu_1 n_2}, \tag{C2a}$$

$$t_{1\to2} = \frac{2\mu_2 n_1}{\mu_2 n_1 + \mu_1 n_2}, \tag{C2b}$$

where n_i is the complex refractive index and μ_i the relative permeability. In practice, the effect of the latter is non-negligible only for iron. However, its permeability depends on the purity of the material and decreases with the saturation of its magnetization. We measured the transmittance of the samples without an external field and, thus, an unknown magnetization state. With $\mu_{Fe} = 10$, the calculated transmittances match at best (2.6 % error for [Pt|Fe|W]$_2$, 4.4 % for [Pt|Fe]$_2$). For the simulations in Fig. 6, we assumed that the Fe layer was fully magnetized and $\mu_{Fe} = 1$, as the magnetic field of the pump is aligned on the OID axis.

Figure 9 shows the resulting spin current and electric field calculated from Eq. (3). We chose Γ_{es} to match the peak frequency of the measurements, since the measured bandwidth is limited by the lowest transverse-optical phonon of ZnTe at 5.3 THz.[44] Using the samples Fe|W(OID) and Fe|Pt(OID) who have a single emitting interface each, we added a factor to the spin-Hall angles to take into account the interface transmission of the spin current through each type of interface, as described by Eq. (5), to match the relative amplitude of the measurements of both samples. We then use a transfer-matrix method as described in Appendix D to calculate the transfer function for the propagation of the THz field from the interface in the sample to after the output surface of the sample. We include the substrate as a layer and model the sample between two half-spaces of air. The thickness of the air layer is set to zero so that we obtain the electric field just outside the sample. We then extracted the transfer function of the THz transport and EOS detection by comparing the complex spectrum of the measured waveform of Fe|W(OID) and the one of its simulated pulse.

TABLE III. Input parameters for the simulation of the three-temperature model.[32,37,42,43]

	Unit	Fe	Pt	W
C_s	J m^{-3} K^{-1}	3400	135	200
C_e	10^6 J m^{-3} K^{-1}	0.2	0.216	0.016
C_l	10^6 J m^{-3} K^{-1}	2.2	2.0746	1
G_{el}	10^6 W m^{-3} K^{-1}	405	40	10
G_{es}	10^6 W m^{-3} K^{-1}	1	1	1
G_{sl}	10^6 W m^{-3} K^{-1}	0.001	0.001	0.001
h	10^6 J^{2}m^{-1} K^{-1}	5	5	5
$\tau_M = C_s/G_{es}$	fs	340	13.5	200
$\tau_e = C_e/G_{sl}$	fs	50	540	160
C_s/G_{sl}	ps	340	135	200
C_e/G_{es}	ps	20	21.6	16

APPENDIX D: TRANSFER MATRIX METHOD

The transfer-matrix method[45,46] is usually used to calculate the one-dimensional propagation of a beam through a structure of thin layers where multiple reflections at the interfaces need to be taken into account. The forward- and backward-propagating field in each layer m is related to the field in the previous layer by the frequency-dependent matrix C_m,

$$\begin{bmatrix} E_{m-1}^+ \\ E_{m-1}^- \end{bmatrix} = C_m \begin{bmatrix} E_m^+ \\ E_m^- \end{bmatrix}, \tag{D1}$$

where

$$C_m(\omega) = \frac{1}{t_m} \begin{bmatrix} e^{i\delta_{m-1}} & r_m e^{i\delta_{m-1}} \\ r_m e^{-i\delta_{m-1}} & e^{-i\delta_{m-1}} \end{bmatrix} \begin{bmatrix} E_m^+ \\ E_m^- \end{bmatrix}, \tag{D2}$$

where r_m and t_m are the Fresnel coefficients at the input interface of the layer and δ_{m-1} the propagation phase through the previous layer. This recurrence relation is usually used to obtain the relation between the field on each side of the sample, i.e., a transfer function for the sample transmission.

However, this assumes that the beam is incoming on the sample, while in the case of spintronic THz emitters, it is generated inside. To represent this, we use a source term S_n as the emitted THz field in layer n. We assume that the THz is emitted directly at the interface. The total field in layer n is then constituted of the source S_n and the back-and-forth-propagating reflections ΔS_n created at the interfaces:

$$\begin{bmatrix} E_n^+ \\ E_n^- \end{bmatrix} = \begin{bmatrix} S_n^+ + \Delta S_n^+ \\ S_n^- + \Delta S_n^- \end{bmatrix}. \tag{D3}$$

The recurrence relation starting in free space before the first layer until layer n takes into account the source emitting backward as well as all reflections. Thus, it does not see the source component emitting forward,

$$\begin{bmatrix} E_0^+ \\ E_0^- \end{bmatrix} = C_1 C_{n-1} C_n \begin{bmatrix} \Delta S_n^+ \\ S_n^- + \Delta S_n^- \end{bmatrix}. \tag{D4}$$

Similarly, the layers after n and until the free space after the last layer M see only the forward-emitting source component and the reflections coming back,

$$\begin{bmatrix} S_n^+ + \Delta S_n^+ \\ \Delta S_n^- \end{bmatrix} = C_{n+1} C_M C_{M+1} \begin{bmatrix} E_{M+1}^+ \\ E_{M+1}^- \end{bmatrix}. \tag{D5}$$

Noting that both E_0^+ and E_M^- are zero as there is no incoming field on the sample, and assuming that $S_n = S_n^+ = S_n^-$ as the charge current emits homogeneously in both directions, the system can be solved. Expressing E_{M+1}^+ as a function of S_n and the components of the multiplied C matrices yields a transfer function between the THz field emitted at the input interface of any layer n and the measured field after the sample.

Since the recurrence relation in Eq. (D1) runs from the first interface of each layer, a numerically safe way to adapt it to sources situated at the other interface of the layer n is to assume instead a source in the layer $n+1$ and add the matrix of the $n|n+1$ interface to the equation.

As our spintronic emitters have THz sources in every NM layer where the ISHE is non-negligible and the fields superpose linearly, we can handle the calculation for each of the sources individually and obtain their respective output fields, which are added or subtracted according to the orientation of the magnetization in the respective FM layers.

Additionally, we implemented a way to approximate the spacial dependency of the sources, as the spin current is progressively converted into charge current over the whole thickness of the layer. We used an exponential decay with a constant corresponding to the inverse mean free path of electrons in the layer.[47] A forward-emitting punctual source situated in layer n at a distance z from the interface would be expressed as $S_n^+(z) = S_n^+(0)\exp(ikz)\exp(-z/\lambda)$ with $S_n^+(0)$ the forward component of the source at the interface and λ the mean free path of the electrons[5] in layer n. The $\exp(ikz)$ term comes from the fact that the shifted source needs to propagate a distance z less until it reaches the next interface. Using this expression in Eq. (D3), one can calculate the field produced at the output of the sample by the source $S_n(z)$. Using this expression in Eq. (D3), one can calculate the field produced at the output of the sample by the source $S_n(z)$. We, thus, discretized the spatial distribution of the THz emission into up to six evenly distributed punctual sources per layer but saw no difference in the numerical result of the calculation. The simulated waveforms presented in the body of the paper were, thus, calculated with a single punctual source at each FM–NM interface.

REFERENCES

[1]T. Kampfrath, M. Battiato, P. Maldonado, G. Eilers, J. Nötzold, S. Mährlein, V. Zbarsky, F. Freimuth, Y. Mokrousov, S. Blügel, M. Wolf, I. Radu, P. M. Oppeneer, and M. Münzenberg, "Terahertz spin current pulses controlled by magnetic heterostructures," Nat. Nanotechnol. **8**, 256–260 (2013).

[2]E. G. Tveten, A. Brataas, and Y. Tserkovnyak, "Electron-magnon scattering in magnetic heterostructures far out of equilibrium," Phys. Rev. B **92**, 180412 (2015).

[3]A. Eschenlohr, L. Persichetti, T. Kachel, M. Gabureac, P. Gambardella, and C. Stamm, "Spin currents during ultrafast demagnetization of ferromagnetic bilayers," J. Phys.: Condens. Matter. **29**, 384002 (2017).

[4]T. Lichtenberg, M. Beens, M. H. Jansen, B. Koopmans, and R. A. Duine, "Probing optically induced spin currents using terahertz spin waves in noncollinear magnetic bilayers," Phys. Rev. B **105**, 144416 (2022).

[5]T. S. Seifert, L. Cheng, Z. Wei, T. Kampfrath, and J. Qi, "Spintronic sources of ultrashort terahertz electromagnetic pulses," Appl. Phys. Lett. **120**, 180401 (2022).

[6]E. Saitoh, M. Ueda, H. Miyajima, and G. Tatara, "Conversion of spin current into charge current at room temperature: Inverse spin-Hall effect," Appl. Phys. Lett. **88**, 182509 (2006).

[7]S. M. Hewett, C. Bull, A. M. Shorrock, C.-H. Lin, R. Ji, M. T. Hibberd, T. Thomson, P. W. Nutter, and D. M. Graham, "Spintronic terahertz emitters exploiting uniaxial magnetic anisotropy for field-free emission and polarization control," Appl. Phys. Lett. **120**, 122401 (2022).

[8]T. Seifert, S. Jaiswal, U. Martens, J. Hannegan, L. Braun, P. Maldonado, F. Freimuth, A. Kronenberg, J. Henrizi, I. Radu, E. Beaurepaire, Y. Mokrousov, P. M. Oppeneer, M. Jourdan, G. Jakob, D. Turchinovich, L. M. Hayden, M. Wolf, M. Münzenberg, M. Kläui, and T. Kampfrath, "Efficient metallic spintronic emitters of ultrabroadband terahertz radiation," Nat. Photon. **10**, 483–488 (2016).

[9]X. Chen, H. Wang, H. Liu, C. Wang, G. Wei, C. Fang, H. Wang, C. Geng, S. Liu, P. Li, H. Yu, W. Zhao, J. Miao, Y. Li, L. Wang, T. Nie, J. Zhao, and X. Wu, "Generation and control of terahertz spin currents in topology-induced 2D ferromagnetic Fe_3GeTe_2—Bi_2Te_3 heterostructures," Adv. Mater. **34**, 2106172 (2022).

[10]Q. Zhang, Y. Yang, Z. Luo, Y. Xu, R. Nie, X. Zhang, and Y. Wu, "Terahertz emission from an exchange-coupled synthetic antiferromagnet," Phys. Rev. Appl. **13**, 054016 (2020).

[11]D. Khusyainov, S. Ovcharenko, M. Gaponov, A. Buryakov, A. Klimov, N. Tiercelin, P. Pernod, V. Nozdrin, E. Mishina, A. Sigov, and V. Preobrazhensky, "Polarization control of THz emission using spin-reorientation transition in spintronic heterostructure," Sci. Rep. **11**, 697 (2021).

[12]D. Kong, X. Wu, B. Wang, T. Nie, M. Xiao, C. Pandey, Y. Gao, L. Wen, W. Zhao, C. Ruan, J. Miao, Y. Li, and L. Wang, "Broadband spintronic terahertz emitter with magnetic-field manipulated polarizations," Adv. Opt. Mater. **7**, 1900487 (2019).

[13]O. Gueckstock, L. Nádvorník, T. S. Seifert, M. Borchert, G. Jakob, G. Schmidt, G. Woltersdorf, M. Kläui, M. Wolf, and T. Kampfrath, "Modulating the polarization of broadband terahertz pulses from a spintronic emitter at rates up to 10 kHz," Optica **8**, 1013 (2021).

[14]X. Wu, H. Wang, H. Liu, Y. Wang, X. Chen, P. Chen, P. Li, X. Han, J. Miao, H. Yu, C. Wan, J. Zhao, and S. Chen, "Antiferromagnetic–ferromagnetic heterostructure-based field-free terahertz emitters," Adv. Mater. **34**, 2204373 (2022).

[15]W. Hoppe, J. Weber, S. Tirpanci, O. Gueckstock, T. Kampfrath, and G. Woltersdorf, "On-chip generation of ultrafast current pulses by nanolayered spintronic terahertz emitters," ACS Appl. Nano Mater. **4**, 7454–7460 (2021).

[16]Y. Liu, Z. Bai, Y. Xu, X. Wu, Y. Sun, H. Li, T. Sun, R. Kong, C. Pandey, M. Kraft, Q. Song, W. Zhao, T. Nie, and L. Wen, "Generation of tailored terahertz waves from monolithic integrated metamaterials onto spintronic terahertz emitters," Nanotechnology **32**, 105201 (2020).

[17]M. Fix, R. Schneider, S. M. de Vasconcellos, R. Bratschitsch, and M. Albrecht, "Spin valves as magnetically switchable spintronic THz emitters," Appl. Phys. Lett. **117**, 132407 (2020).
[18]R. Rouzegar, L. Brandt, L. Nadvornik, D. A. Reiss, A. L. Chekhov, O. Gueckstock, C. In, M. Wolf, T. S. Seifert, P. W. Brouwer, G. Woltersdorf, and T. Kampfrath, "Laser-induced terahertz spin transport in magnetic nanostructures arises from the same force as ultrafast demagnetization," arXiv:2103.11710 [cond-mat] (2021).
[19]Y. Hoshi, E. Suzuki, and M. Naoe, "Uniaxial magnetic anisotropy of iron thin films deposited by oblique incidence of deposition particles," J. Appl. Phys. **79**, 4945–4947 (1996).
[20]K. Okamoto, T. Hashimoto, K. Hara, and E. Tatsumoto, "Origin of magnetic anisotropy of iron films evaporated at oblique incidence," J. Phys. Soc. Jpn. **31**, 1374–1379 (1971).
[21]K. Schlage, L. Bocklage, D. Erb, J. Comfort, H.-C. Wille, and R. Röhlsberger, "Spin-structured multilayers: A new class of materials for precision spintronics," Adv. Funct. Mater. **26**, 7423–7430 (2016).
[22]S. Willing, K. Schlage, L. Bocklage, M. M. Ramin Moayed, T. Gurieva, G. Meier, and R. Röhlsberger, "Novel tunnel magnetoresistive sensor functionalities via oblique-incidence deposition," ACS Appl. Mater. Interfaces **13**, 32343–32351 (2021).
[23]J. D. Jackson, *Classical Electrodynamics*, 3rd ed. (Wiley, New York, 1999).
[24]G. Li, R. Medapalli, R. V. Mikhaylovskiy, F. E. Spada, T. Rasing, E. E. Fullerton, and A. V. Kimel, "THz emission from Co/Pt bilayers with varied roughness, crystal structure, and interface intermixing," Phys. Rev. Mater. **3**, 084415 (2019).
[25]T. Seifert, S. Jaiswal, M. Sajadi, G. Jakob, S. Winnerl, M. Wolf, M. Kläui, and T. Kampfrath, "Ultrabroadband single-cycle terahertz pulses with peak fields of 300 kV cm^{-1} from a metallic spintronic emitter," Appl. Phys. Lett. **110**, 252402 (2017).
[26]R. Schneider, M. Fix, J. Bensmann, S. M. de Vasconcellos, M. Albrecht, and R. Bratschitsch, "Spintronic GdFe/Pt THz emitters," Appl. Phys. Lett. **115**, 152401 (2019).
[27]D. M. Nenno, L. Scheuer, D. Sokoluk, S. Keller, G. Torosyan, A. Brodyanski, J. Lösch, M. Battiato, M. Rahm, R. H. Binder, H. C. Schneider, R. Beigang, and E. T. Papaioannou, "Modification of spintronic terahertz emitter performance through defect engineering," Sci. Rep. **9**, 13348 (2019).
[28]J.-G. Wang, J.-D. Shao, S.-M. Wang, H.-B. He, and Z.-X. Fan, "Form birefringence in thin films with oblique columnar structures," Chinese Phys. Lett. **22**, 2066–2068 (2005).
[29]A.-L. Calendron, J. Meier, E. Kueny, S. Velten, L. Bocklage, R. Röhlsberger, and F. X. Kärtner, "Bulk, cascaded pulse compression scheme and its application to spin emitter characterization," Appl. Opt. **60**, 912–917 (2021).
[30]G.-M. Choi, B.-C. Min, K.-J. Lee, and D. G. Cahill, "Spin current generated by thermally driven ultrafast demagnetization," Nat. Commun. **5**, 8 (2014).
[31]N. Medvedev and I. Milov, "Electron-phonon coupling in metals at high electronic temperatures," Phys. Rev. B **102**, 064302 (2020).
[32]R. Chimata, A. Bergman, L. Bergqvist, B. Sanyal, and O. Eriksson, "Microscopic model for ultrafast remagnetization dynamics," Phys. Rev. Lett. **109**, 157201 (2012).
[33]A. Kirilyuk, A. V. Kimel, and T. Rasing, "Ultrafast optical manipulation of magnetic order," Rev. Mod. Phys. **82**, 2731–2784 (2010).
[34]S. J. Byrnes, "Multilayer optical calculations," arXiv:1603.02720 (2016).
[35]K. E. Oughstun and C. L. Palombini, "Fresnel reflection and transmission coefficients for temporally dispersive attenuative media," Radio Sci. **53**, 1382–1397 (2018).
[36]A. Fernandez-Pañella, T. Ogitsu, K. Engelhorn, A. A. Correa, B. Barbrel, S. Hamel, D. G. Prendergast, D. Pemmaraju, M. A. Beckwith, L. J. Bae, J. W. Lee, B. I. Cho, P. A. Heimann, R. W. Falcone, and Y. Ping, "Reduction of electron-phonon coupling in warm dense iron," Phys. Rev. B **101**, 184309 (2020).
[37]A. P. Caffrey, P. E. Hopkins, J. M. Klopf, and P. M. Norris, "Thin film non-noble transition metal thermophysical properties," Microscale Thermophys. Eng. **9**, 365–377 (2005).
[38]J. W. Arblaster, "Thermodynamic properties of tungsten," J. Phase Equilib. Diffus. **39**, 891–907 (2018).
[39]T. S. Seifert, N. M. Tran, O. Gueckstock, S. M. Rouzegar, L. Nadvornik, S. Jaiswal, G. Jakob, V. V. Temnov, M. Münzenberg, M. Wolf, M. Kläui, and T. Kampfrath, "Terahertz spectroscopy for all-optical spintronic characterization of the spin-Hall-effect metals Pt, W and $Cu_{80}Ir_{20}$," J. Phys. D: Appl. Phys. **51**, 364003 (2018).
[40]C. Guillemard, S. Petit-Watelot, S. Andrieu, and J.-C. Rojas-Sánchez, "Charge-spin current conversion in high quality epitaxial Fe/Pt systems: Isotropic spin Hall angle along different in-plane crystalline directions," Appl. Phys. Lett. **113**, 262404 (2018).
[41]C.-F. Pai, L. Liu, Y. Li, H. W. Tseng, D. C. Ralph, and R. A. Buhrman, "Spin transfer torque devices utilizing the giant spin Hall effect of tungsten," Appl. Phys. Lett. **101**, 122404 (2012).
[42]D. Gall, "Electron mean free path in elemental metals," J. Appl. Phys. **119**, 085101 (2016).
[43]R. Freeman, A. Zholud, Z. Dun, H. Zhou, and S. Urazhdin, "Intrinsic and extrinsic contributions to spin scattering in Pt," Phys. Rev. Lett. **120**, 067204 (2018).
[44]S. Casalbuoni, H. Schlarb, B. Schmidt, P. Schmüser, B. Steffen, and A. Winter, "Numerical studies on the electro-optic detection of femtosecond electron bunches," Phys. Rev. ST Accel. Beams **11**, 072802 (2008).
[45]O. S. Heavens, *Optical Properties of Thin Solid Films* (Dover Publications, New York, 1965).
[46]F. Abelès, "La théorie générale des couches minces," J. Phys. Radium **11**, 307–309 (1950).
[47]O. Gueckstock, L. Nádvorník, M. Gradhand, T. S. Seifert, G. Bierhance, R. Rouzegar, M. Wolf, M. Vafaee, J. Cramer, M. A. Syskaki, G. Woltersdorf, I. Mertig, G. Jakob, M. Kläui, and T. Kampfrath, "Terahertz spin-to-charge conversion by interfacial skew scattering in metallic bilayers," Adv. Mater. **33**, 2006281 (2021).